Table of Contents

1. Fabrication of nanoporous Si (or Mg foil) trench

Nanoporous Si (np-Si) and Mg foil served as mechanical supports for microelectromechanical systems (MEMS). Free-standing np-Si (~80 μm thick) was prepared from double-side polished, highly doped p-type Si wafers (0.001-0.005 Ω·cm, University Wafers, USA) at a current density 160 mA·cm^{-2}, as previously reported.[1] Lamination delivers the np-Si onto a layer of PDMS spin cast on a glass slide, for deposition of SiO_2 (~300 nm) by PECVD. Patterning and etching of the SiO_2 and np-Si yielded a trench in the np-Si. As an alternative to np-Si, a commercial Mg foil (~100 μm thick, Goodfellow, USA) can be thinned, patterned, and wet etched by a mixture of acetic acid (CH_3COOH, Transene Company Inc., USA) and deionized (DI) water (20 ml: 250 ml), to create a trench (~40 μm depth) in the processed Mg foil (~80 μm thick). The PLGA is transfer printed on the np-Si (or Mg foil) with a micro-tip patterned PDMS stamp.[2] The manufactured devices on PLGA substrates were then integrated with np-Si (or Mg foil) near the glass transition temperature (T_g, ~65 °C) for 5 min on a hot plate.

2. Calibration of biodegradable biosensors

Accelerometer — Calibration involved measurements of a biodegradable accelerometer and a commercial device (NeuLog, USA) moved rapidly up and down in the vertical direction. The calibration approach to connect measured changes in resistance to acceleration was similar to that used for the pressure sensor. *Temperature sensor* — Real-time measurements of the change in resistance of a biodegradable sensor and of temperature using a commercial sensor (NeuLog, USA) submerged in ACSF yielded the

calibration curves (Fig. S10). ***Flow meter*** — The device was placed in a water bath with constant flow rate. While 1 mA (DC current source; Model 6220, Keithley, USA) was applied to the thermal actuator, the resistances of the two temperature sensors were measured using a data acquisition (DAQ) system (USB-4065, National Instruments, USA). ***Thermal conductivity/diffusivity sensor*** — The thermal conductivity of an aqueous solution was measured as follows. A current (500 µA) was supplied to the resistive element by a programmable DC current source (Model 6220, Keithley, USA) for 1 s. The time-dependent voltage across the element was then sampled at 100 V/s using a 22-bit programmable digital multimeter (USB-4065, National Instruments, USA). The voltage and current values allowed calculation of the time-dependent resistance of the device, which, in turn, is proportional to temperature. ***pH sensor*** — Si nanoribbons (Si NRs) were exposed by ultraviolet induced ozone for 3 min and immersed in a 1% ethanol solution of 3-aminopropyltriethoxysilane (APTES, Sigma-Aldrich, USA) for 20 min. After thorough rinsing with ethanol three times, Si NRs were annealed at 60°C for 10 min to functionalize their surfaces. An Ag/AgCl reference electrode was placed in the center of the solutions, and a floating gate voltage defined the quiescent conductance of the Si NRs. Changes in conductance were measured during partial immersion of the device in phosphate buffer solution (Sigma Aldrich, USA) with various pH between 2 and 10. After a short period of stabilization, a semiconductor analyzer (4155C, Agilent, USA) recorded the conductance of the Si NRs for ~50 s in the solutions.

3. Operating principles of mechanical/physical/chemical sensors

Pressure sensor — The deformable diaphragm structure in Figure 1a provides a highly sensitive pressure response.[3,4] The average strain in the Si-NM serpentine structure on PLGA induced by applied pressure causes a piezoresistive electrical response. Under intracranial pressure, both the np-Si mechanical support and PLGA diaphragm would deform. Three-dimensional finite element analysis (3D-FEA), however, suggests that the deformation of the np-Si mechanical support is negligible in comparison to that of PLGA diaphragm, indicating a reasonable simplification to clamp all four edges of PLGA diaphragm in the current study.[5] In the numerical analysis, an 8-node hexahedral solid element C3D8R and a quadrilateral shell element S4R were used for the diaphragm and Si-NM piezoresistive sensor, respectively. The ideal elastic constitutive relation describes the mechanical behavior of the Si and PLGA. To maximize the sensor sensitivity (i.e., average strain in the Si-NM piezoresistive sensor) to applied pressure, the center of the edge of the diaphragm was chosen as the location for the sensor. The average strain at different positions of diaphragm shown in Fig. S5 rationalizes this choice. The sensitivity also depends on the size of PLGA diaphragm. For a given area, 3D-FEA results indicate that the optimum is achieved when the PLGA diaphragm is close to a square in shape (see Fig. S6). Fig. S7 provides a comparison of experimental and FEA results for change in resistance with pressure. The following equation provides the relationship between the change in resistance due to piezoresistivity through a gauge factor (G):

$$R = R_0\left(1 + G\varepsilon\right), \tag{1}$$

where ε is the average strain on the piezoresistive sensor, and R and R_0 are the change in resistance and resistance at zero pressure, respectively. Here, the average strain was calculated from 3D-FEA for pressure ranging from 0 to 70 mmHg. With R_0 as 249

kΩ, the gauge factor was estimated to be ~30.   ***Accelerometer*** — The pressure sensor platform can serve as an accelerometer where the sensor consists of a cantilever with a rigid proof mass m attached at its distal end (Fig. S11).   Under a given acceleration a, the force experienced by the proof mass generates a bending moment at the fixed end of the beam, $M = mad$, where d is the distance from the center of the proof mass to the fixed end.   This results in a strain at the location where Si-NM piezoresistive coil resides $\varepsilon = Mt/(2EI)$, where $EI = Ewt^3/12$ is the bending stiffness of the cantilever, and w and t are the width and thickness of the cantilever, respectively.   Taken together with Equation (1), the acceleration sensitivity is tunable by changes of the elastic properties and the geometry via the following relationship $a = \Delta R/R\left(Ewt^2\right)/(6Gmd)$.[3,6]   ***Temperature sensor*** — The resistance (or conductance) changes by an amount linearly proportional to temperature, according to:

$$R = R_0\left(1 + \alpha(T - T_0)\right) \tag{2}$$

where R and R_0 are the changed resistance and initial resistance, T and T_0 are the measured and initial temperatures, and α is the temperature coefficient of resistance (TCR).   The TCR in Figure 1h is 1×10^{-4}, where doped Si has various TCR ranges depending on the type of dopants and doping concentration.[7]   A larger initial resistance increases the absolute change in resistance.   As a result, highly dense serpentines, which dominate the total resistance, were adopted for the temperature sensors (see Fig. S12).   ***Flow rate monitor*** — The flow rate monitor consists of one thermal actuator and two temperature sensors (see Fig. S14).   The thermal actuator is placed in the middle of two temperature sensors, along the flow direction.   When the actuator generates heat, a temperature difference appears between two temperature sensors, due

to heat transfer mediated by the flow.[8]   The difference in temperature can be quantitatively correlated to flow rate.   ***Thermal conductivity/diffusivity sensor*** — A sudden increase of the power applied to the resistive element induces a temperature increase in the resistor due to Joule heating.   The time dynamics of the temperature increase is, in part, a function of the thermal transport properties of the surrounding fluid.   As a result, analysis of the temperature transients immediately following the power increase allows determination of the thermal transport properties of the surrounding fluid or tissue.[9]   ***pH sensor*** — The functionalized surfaces of Si-NRs with both $-NH_2$ and $-SiOH$ groups undergo protonation to $-NH_3^+$ at low pH and deprotonation to $-SiO^-$ at high pH.[10-12] The resulting changes in the surface charge electrostatically gate the transport in the Si-NRs by depleting or accumulating charge carriers, resulting in a stepwise decrease in the conductance of the phosphorous-doped Si-NRs as the pH in aqueous solutions increases from 2 to 10 in distinct steps (see Fig. S15 for Si pH sensor).

4. Temperature effects on piezoresistivity of pressure sensors

Temperature affects the resistance and the coefficient of piezoresistivity.[7] Therefore, calibration of these effects in piezoresistive-type pressure sensors enhances the accuracy of the pressure measurements.   The temperature effect on resistance is described by Equation (2) in the previous section through the temperature coefficient of resistance (TCR, α).   The temperature effect on piezoresistivity is described by the temperature coefficient of piezoresistivity (TCP, β)

$$\pi = \pi_0\left(1 + \beta\left(T - T_0\right)\right), \tag{3}$$

where π and π_0 are the final and initial piezoresistivity coefficients, and T and T_0 are the measured and initial temperatures, respectively. The temperature coefficient of piezoresistivity β of Si varies, depending on the dopants and doping concentration.[7] Assuming the piezoresistivity is directly proportional to the gauge factor (G), the strain (ε) can be correlated with resistance (TCP) as

$$R_{(T,P)} = R_{(T,P=0)}\left(1+G\varepsilon\right) = R_{(T=0,P=0)}\left[1+\alpha\left(T-T_0\right)\right]\left\{1+G_0\left[1+\beta\left(T-T_0\right)\right]\varepsilon\right\} \quad (4)$$

where $R_{(T,P)}$ is the final resistance affected by temperature and pressure, $R_{(T,P=0)}$ is the resistance when only temperature is applied, $R_{(T=0,P=0)}$ is the initial resistance without changes in pressure nor temperature (usually 20 or 25 °C), G and G_0 are the final and initial gauge factors. With predetermined α, β, G_0 and $R_{(T=0,P=0)}$, the temperature effects on the resistance and piezoresitivity can be calibrated. Fig. S19 shows the resistance vs. pressure curve at the different temperatures measured by transient pressure sensors, giving $\alpha=0.5\times10^{-3}$ and $\beta=-2.2\times10^{-3}$. It should be noted that a typical range of β of p-type Si is -2.7×10^{-3} to -1.6×10^{-3}, for doping concentration between 5×10^{18} and 1×10^{20}/cm^3.[7] Here the change in pressure sensitivity due to temperature change in this intracranial study (±5 °C) is about 1%, and hence negligible. The following simplified equation can then be used to calibrate the temperature effect on the base resistance:

$$R_{(T,P)} = R_{(T=0,P=0)}\left[1+\alpha\left(T-T_0\right)\right]\left(1+G_0\varepsilon\right). \quad (5)$$

Optimizing the doping concentration to increase the sensitivity to pressure and minimize sensitivity to temperature, and/or using a Wheatstone-bridge type of design with four piezoresistive elements, are alternative routes to minimize the temperature effect.[3,4]

5. Animal behavior test with percutaneous wires

The novel object recognition (NOR) task is used to evaluate cognition, particularly recognition memory, in rodent models of CNS disorders. We tested 6 controls and 6 rats with implanted percutaneous wires and their spontaneous tendency to spend more time exploring a novel object than a familiar one. The choice to explore the novel object reflects the use of learning and recognition memory. We observed no significant change in those with precautions implants as opposed to controls as shown in Figure S31.

6. *In vivo* implantation of bioresorbable wireless monitors for intracranial pressure and temperature

Animals were anesthetized and held in a stereotaxic frame after analgesia and antibiotic prophylaxis. Incising along the dorsal midline of the head longitudinally and retracting the scalpallowed the visualization of bregma and lamdba. The craniectomy was fashioned utilizing a high speed drill on the right side of the rat's skull over somatosensory cortex. After placing the transient biosensors on the cortical surface, small pieces of saline soaked absorbable gelatin compressed sponge (Gelfoam®, Pfizer, USA) were applied. For the fully implantable NFC system, the craniectomy defect was sealed by degradable surgical glue (TISSEEL, Baxter Healthcare Co., USA), and the NFC system was placed on the outside surface of the skull. A subgaleal closure utilizing interrupted resorbable sutures sealed the surgical site with all device components fully implanted. For the transcutaneous bioresorbable wiring method,

placing a PLGA sheet on the skull by covering the craniectomy defect and bonding the sides by degradable surgical glue formed the closed intracranial cavity while the wires were withdrawn outside. Finally, a subgaleal closure utilizing interrupted resorbable sutures while laying degradable wires out provides the fully resorbable interfaces with dissolvable metal wires. The plastic hat, which provides the protection from rat's movement and handling, was bonded on the sutured region with an epoxy. Placing a wireless transmitter (Pinnacle 8151 fixed-frequency 2-channel wireless potentiostat, Pinnacle Technology, USA) with connection of the degradable wires in the plastic hat allows the long range (>10 m) wireless monitoring of pressure and/or temperature. The battery-powered potentiostat delivered a 0.6 V potential to each channel at a 1 Hz sampling frequency, measured and amplified the delivered current with a gain of 100,000 digitized the reading, and transmitted the value over a 900 MHz wireless protocol to a computer-connected base station. Implanting a standard clinical ICP monitor, (Integra LifeSciences Co., USA) near the dissolvable sensor and sealing with a silicone polymer enabled the comparison of resorbable pressure sensor with a clinical ICP monitor. The commercial thermistor (DigiKey Electronics, USA) implanted at the site near the resorbable temperature sensor and plugged to a wireless transmitter provided the parallel monitoring of brain temperature with resorbable sensor. Post-operative care procedure based on the local protocol of the animal welfare regulations providing the rat's reasonable recovery and health movement in single-housed cage.

7. Characterization of the near-field communication (NFC) system

The NFC chip operates using power delivered wirelessly by inductive coupling. The regulated working voltage ranges from 1.45 to 1.65 V. The chip includes a microcontroller (MSP430), with 2kB, 4kB and 8kB of FRAM, SRAM and ROM, respectively. The system supports four channels of Sigma-Delta analog to digital converters, each with 14 bit resolution. The phase, impedance, and resonance frequency of the fully implantable NFC system was evaluated by near field coupling to a coil connected to an impedance analyzer (Agilent 4191A RF Impedance Analyzer, Agilent, USA). A signal generator (Keithley 3390, Keithley, USA) provides 10 Hz sine, square, ramp wave inputs to the NFC system, The input of the signal generator and the wireless measured signals from the NFC system were compared to assess the high speed acquisition capabilities. Finite impulse response filters were loaded into the chip and frequency responses were acquired by using the signal generator to produce sine wave inputs with frequencies between 0.1 to 20Hz.

8. Synthesis/hydrolysis chemistry, dissolution kinetics, water permeability, biocompatibility of polyanhydride encapsulation

A biodegradable polyanhydride, PBTPA (poly buthanedithiol 1,3,5-triallyl-1,3,5-triazine-2,4,6(1H,3H,5H)-trione pentenoic anhydride), was synthesized and used as an organic encapsulant, capable of defining the lifecycle of device operation by controlling the water diffusion. Thiol-ene click-chemistry was used for the construction of degradable polyanhydride. Mixture of 1 mole of 4-pentenoic anhydride (4PA), 4 mole of 1,3,5-triallyl-1,3,5-triazine-2,4,6(1H,3H,5H)-trione (TTT)

and 7 mole of 1,4-butanedithiol was polymerized by UV light for an hour with the addition of 2-hydroxy-4'-(2-hydroxyethoxy)-2-methylpropiophenone as the photoinitiator (total mass of 0.1%), yielding biodegradable PBTPA with hydrophobic chains (see Fig. S23). Here, 4PA and TTT act as a degradable linker and hydrophobic component, respectively, and butanedithiol crosslinks both 4PA and TTT through UV induced thiol-ene reaction.

Fig. S24a shows the hydrolysis kinetics of polyanhydride at the different solution pH at room temperature, 0.5, 1.2, 2.8 mg/day for pH 6.7, 7.4, and 8 solutions. Since anhydride bonds can be hydrolyzed giving two hydrophilic carboxylic acid bonds, PBTPA tends to gradually collapse and dissolve into water (see Fig. S23). The water permeability can be tracked by a simple water-sensitive electrical element, i.e. an Mg resistor in this study. The resistance of the Mg resistor increases if the water diffuses to the Mg and begins to dissolve it. Details of this type of test method appear elsewhere.[13,14] Fig. S24b shows the resistance at various times for a Mg resistor (~300 nm thick) encapsulated with polyanhydride (~120 μm). The Resistance is stable until 4 days and then starts to increase significantly, implying the Mg resistor has dissolved. Polyanyhdride provides a barrier to water diffusion to control the operating lifetime of the pressure sensor. This type of electrical degradation is observed in the encapsulation of the interconnecting electrodes (Mo). Fig. S27 shows the degradation of electrical function of biodegradable wires (Mo, Mg) and interconnecting electrode (Mo) measured without encapsulation. The Mg wires are stable for about 5 days (change of less than 3 Ω) but then shows large changes in resistance, due to their increased rate of dissolution compared to Mo (which shows a much smaller resistance change, ~3 Ω). The Mo electrode parts dissolve within a few hours without encapsulation.

Polyanhydride encapsulation enhances the stable operation time of Mo to six days with less than 10 Ω change.   At 7 days the water begins to dissolve the Mo interconnection significantly and the resistance increases to ~50 Ω.

An additional layer of encapsulation on the PLGA membrane affects the mechanics of deformation, thereby changing the calibration. Fig. S22a indicates a change from 82 to 50 Ω/mmHg via the addition of a 120 μm thick coating of polyanyhydride. Fig. S22b summarizes results of FEA simulation, consistent with this observation.   The average strain in the Si-NM sensor reduces with the addition of the encapsulation.   The balance between sensitivity and operational lifecycle can be managed through appropriate selection of trench geometry, Si-NM width, modulus and thickness of the membrane and the encapsulation layer, and the water permeation (chemistry and thickness of encapsulation).

Pieces of polyanhydride (10 mm $\times$ 3 mm) and HDPE (High-density polyethylene, negative control sample) were implanted subcutaneously in Balb/c mice to assess the toxicity. Fig. S25 provides hematoxylin and eosin (H&E) images of tissue around the implant sites for polyanyhdride and HDPE after 14 days.   Histologic examination showed that inflammatory cell infiltration and fibrosis in surrounding tissues were no different with negative control groups.   There were no obvious signs of local toxicity caused by polyanhydride or its by-products as results were comparable to the HDPE group.

9. Immunohistochemistry

Immunohistochemistry was performed as described previously, with minor modifications.[15,16] The two types of bioresorbable pressure sensors (np-Si and Mg foil structure) were placed on the cortex in the craniectomy site on the right hemisphere above the sensory motor cortex for 2 weeks, 4 weeks, and 8 weeks. A craniectomy is performed on the left side again above the sensorimotor cortex and the dura is opened above the sensorimotor cortex but no implant is placed. This acts as a histological control to the right side with the implant placed. Brain slices are double-immunostained for GFAP (glial fibrillary acidic protein) to detect astrocytes and Iba1 (ionized calcium-binding adapter molecule 1) to identify microglia/macrophages. Briefly, rats are anesthetized and intracardially perfused with ice-cold 4% paraformaldehyde in phosphate buffer (PB). Brains are carefully dissected with particular attention to preserve the right cortical surface beneath the now fully resorbed device and the left cortical surface acting as a control. Brains are post-fixed 2 hr at 4 ℃ and cryoprotected with solution of 30% sucrose in 0.1M PB at 4℃ for at least 4 d, cut into 30 μm sections and processed for immunostaining. 30 μm brain sections are washed three times in PBS and blocked for one hour in PBS containing 0.5% Triton X-100 and 5 % normal goat serum. Sections are then incubated for 16 hr at 4℃ in guinea pig anti-GFAP (1:500, Synaptic Systems 173 004) and rabbit anti-Iba1 (1:300, Wako Chemicals 019-19741). Following incubation, sections are washed three times in PBS and then incubated for 2 hr at room temperature in Alexa fluor 488 goat anti-rabbit IgG (1:1000, Life Technologies A11008) and Alexa fluor 546 goat anti-guinea pig IgG (1:1000, Life Technologies A11074). Sections are then washed three times in PBS and then incubated for 1 hr at room temperature in NeuroTrace® 435/455 Blue Fluorescent Nissl Stain (Life Technologies N21479) in PB (1:400). Sections are then washed three times in

PBS followed by three washes in PB and mounted on glass slides with HardSet Vectashield (Vector Labs) for microscopy. All sections imaged on a digital slide scanner (Olympus NanoZoomer HT model). Gain and exposure time are digitally set and constant throughout. Images corresponding with the right cortical surface interfacing with the device are compared with the left control cortical surface which did not have a device implanted. Gliosis is compared between cortex underlying the now resorbed implant and the control.

10. Other applications of bioresorbable pressure sensors

Sensors implanted at the intra-abdominal cavity and lower extremities demonstrated the versatility usages in implantable biomedical applications. The abdominal wall was shaved and prepped at the incision site with 70% ethanol. Animals were subjected to a 4 cm full-thickness median incision along the linea alba, using the xiphoid process as the reference point by a sterile technique.   After abdominal incision, the transient pressure sensor and clinical pressure sensor were placed in the abdominal cavity amongst the abdominal viscera. A modified roman sandal technique using a 3/0 VICRYL RAPIDE (polyglactin 910) suture secured the sensor and the abdomen was closed with simple interrupted 3/0 VICRYL RAPIDE (polyglactin 910) sutures. Manual abdominal compression yielded the increase of intra-abdominal pressure. A small (~5 mm) vertical incision was made along the thigh using scissors, and the skin was retracted laterally to implant the pressure sensor into extremities cavity. The muscles of the posterior thigh (including the hamstring

muscles) were split, and the biodegradable pressure sensor and commercial sensor were placed in the musculofascial compartment. The implants were secured utilizing the same method as the abdominal surgery.

11. Injectable biodegradable sensors

A three-axis vertical stereotactic frame and arm temporary tied with an injectable device allowed accurate positioning and stable injection into the deep brain site. Adjustments of the jig enabled the needle system to penetrate into brain tissue via a square hole in the skull of a rat. Release of the needle device completed implantation, followed by sealing the skull with a silicone polymer (Kwik-Sil, World Precision Instruments Inc., USA) and dental acrylic. A manual increase in pressure induced by compressing the abdomin provided a means to compare the bioresorbable needle pressure sensor to a commercial device injected at an adjacent location. Monitoring the temperature during the anesthetization and recovery yielded data to compare the bioresorbable temperature sensor to temperatures measured by infrared imaging on the surface of brain.

12. Characterizations of porosity and average pore size of nanoporous silicon (np-Si)

The porosity of the np-Si was characterized by optical reflectance spectroscopy. The refractive index of np-Si (n) was determined as ~1.55 from the spacing of adjacent maxima in the Fabry-Perot oscillations in the reflectance spectrum (~1.3 to 1.6 μm)

using[17]

$$n = \frac{1}{2d} \cdot \frac{1}{\left(\dfrac{1}{\lambda_1} - \dfrac{1}{\lambda_2} \right)} \qquad , \tag{6}$$

where λ_1 and λ_2 are the local maximum and the adjacent, longer-wavelength local maximum in the reflectance spectrum, and d is the thickness of np-Si determined by scanning electron microscope (SEM). The porosity was determined by using the calculated n and the two-component Bruggeman effective medium approximation:[18]

$$\phi \left(\frac{1 - n^2}{1 + 2n^2} \right) + (1 - \phi) \left(\frac{n_{Si}^2 - n^2}{n_{Si}^2 + 2n^2} \right) = 0 \qquad , \tag{7}$$

where ϕ and n_{Si} are the porosity of np-Si and the real part of the refractive index of bulk Si, respectively.[19] Assuming a Si bulk refractive index of 3.5, the porosity of np-Si is ~70.5%. This agrees well with gravimetric porosity measurements (i.e. relative mass of np-Si film to mass of bulk Si that would occupy the same geometric volume), which suggest an average porosity of $69 \pm 3\%$.

The average pore size was determined using a gas sorption system (NOVA $-e$ Series, Quantachrome Instruments). np-Si membranes were subjected to both nitrogen adsorption and desorption measurements. The sorption system's NovaWin software applied the Barrett, Joyner, and Halenda (BJH) Method[20] to the experimental isotherms, resulting in an average pore size of 12 ± 3 nm, which is in agreement with what is observed in the top view image from the scanning electron microscope.

References

1. Ning, H. *et al.* Transfer-Printing of Tunable Porous Silicon Microcavities with Embedded Emitters. *ACS Photonics* **1**, 1144–1150 (2014).

2. Wu, J. *et al.* Mechanics of reversible adhesion. *Soft Matter* **7**, 8657-8662 (2011).

3. Liu, C. *Foundations of MEMS* Ch. 6 (Prentice Hall, London, 2011).

4. Sugiyama, S., Takigawa, M., Igarashi, I. Integrated Piezoresistive Pressure Sensor with Both Voltage and Frequency Output. *Sens. and Actuators A* **4**, 113–120 (1984).

5. Wang, C.-T., *Nonlinear large-deflection boundary-value problems of rectangular plates*. (DTIC Document, 1984).

6. Angell, J.B., Terry, S. C., Barth, P.W. Silicon Micromechanical Devices. *Sci. Am. J.* **248**, 44–55 (1983).

7. Hsu, T. R. *MEMS & Microsystems: Design, Manufacture, and Nanoscale Engineering* Ch. 7 (John Wiley & Sons, Inc., Hoboken, New Jersey, USA, 2008).

8. Van der Horst, A. *et al.* A Novel Flexible Thermoelectric Sensor for Intravascular Flow Assessment. *IEEE Sens. J.* **13**, 3883-3891 (2013).

9. Webb, R. C. *et al.* Ultrathin Conformal Devices for Precise and Continuous Thermal Characterization of Human Skin. *Nature Mater.* **12**, 938-944 (2013).

10. Vezenov, D. V., Noy, A., Rozsnyai, L. F., Lieber, C. M. Force titrations and ionization state sensitive imaging of functional groups in aqueous solutions by chemical force microscopy. *J. Am. Chem. Soc.* **119**, 2006-2015 (1997).

11. Cui, Y.; Wei, Q. Q.; Park, H. K.; Lieber, C. M. Nanowire Nanosensors for Highly-Sensitive, Selective and Integrated Detection of Biological and Chemical Species. *Science* **293**, 1289-1292 (2001).

12. Penner, R. M. Chemical sensing with nanowires. *Annu. Rev. Anal. Chem.* **5**, 461-485 (2012).

13. Hwang, S.-W. *et al*. A Physically Transient Form of Silicon Electronics. *Science* **337**, 1640-1644 (2012).

14. Kang, S.-K. *et al*. Dissolution Behaviors and Applications of Silicon Oxides and Nitrides in Transient Electronics. *Adv. Func. Mater.* **24**, 4427-4434 (2014).

15. M. R. Bruchas et al., Selective p38α MAPK deletion in serotonergic neurons produces stress resilience in models of depression and addiction. *Neuron* **71**, 498-511 (2011).

16. Kim, T. I. *et al*. Injectable, Cellular-Scale Optoelectronics with Applications for Wireless Optogenetics. *Science* **240**, 211-216 (2013).

17. Gaber, N., Khalil, D. & Shaarawi, A. Fabrication of optical filters using multilayered porous silicon. in Advanced Fabrication Technologies for Micro/Nano Optics and Photonics IV 7927, 79270S–79270S–9 (2011).

18. Bosch, S., Ferré-Borrull, J., Leinfellner, N. & Canillas, A. Effective dielectric function of mixtures of three or more materials: a numerical procedure for computations. Surf. Sci. 453, 9–17 (2000).

19. Schmid, P. E. Optical absorption in heavily doped silicon. Phys. Rev. B 23, 5531–5536 (1981).

20. Barrett, E. P., Joyner, L. G. & Halenda, P. P. The Determination of Pore Volume and Area Distributions in Porous Substances. I. Computations from Nitrogen Isotherms. *J. Am. Chem. Soc.* **73,** 373–380 (1951).

21. Kang, S. K. *et al.* Biodegradable Thin Metal Foils and Spin-On Glass Materials for Transient Electronics, *Adv. Func. Mater.* **25**, 1789-1797 (2015).

22. Yin, Y. *et al*. Dissolvable Metals for Transient Electronics. *Adv. Func. Mater.* **24**, 645-658 (2014).

Table S1. Hydrolysis mechanisms and dissolution rates of key materials in this study (ACSF and PBS measured at 37 °C, DI at room temperature).

Materials	Dissolution rate (nm/day)			Hydrolysis mechanism
	ACSF	PBS[12,21]	DI[22]	
Si NM	2.3×10^1	0.5×10^1		$Si + 4H_2O \rightarrow Si(OH)_4 + 2H_2$
np-Si	9.0×10^3	-	-	
SiO$_2$	0.8×10^1	1.4×10^1		$SiO_2 + 2H_2O \rightarrow Si(OH)_4$
Mg	4.0×10^3	-	1.7×10^3	$MgO + H_2O \rightarrow Mg(OH)_2$
Mo	-	2.0×10^1	0.7×10^1	$2Mo + 2H_2O + 3O_2 \rightarrow 2H_2MoO_4$
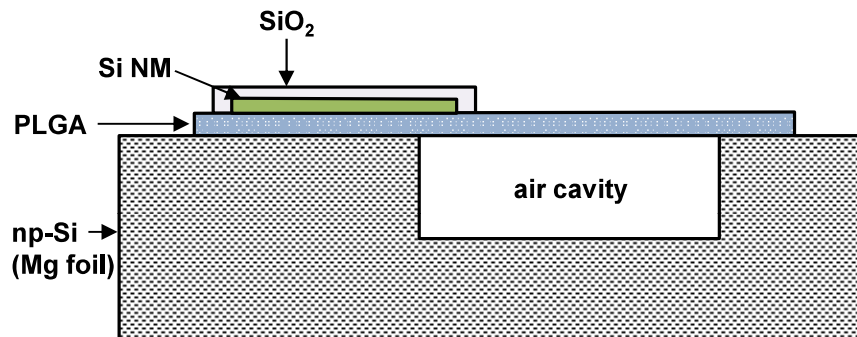
Figure S1. Cross-sectional side view of the bioresorbable pressure sensor.
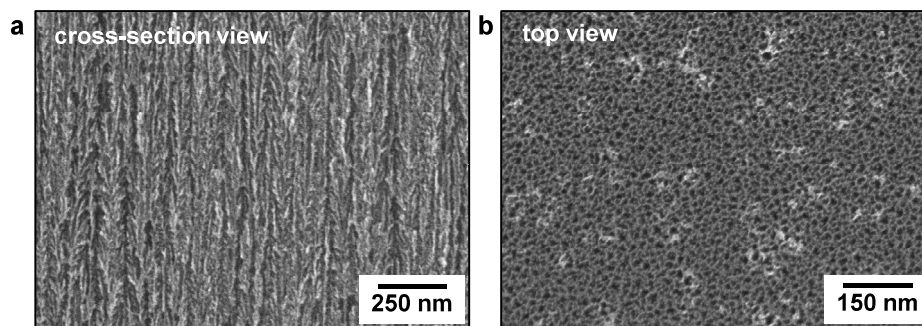
Figure S2. Scanning electron microscope (SEM) images of nanoporous Si. a) Cross-section view and b) top view of np-Si structure with ~71 % porosity.
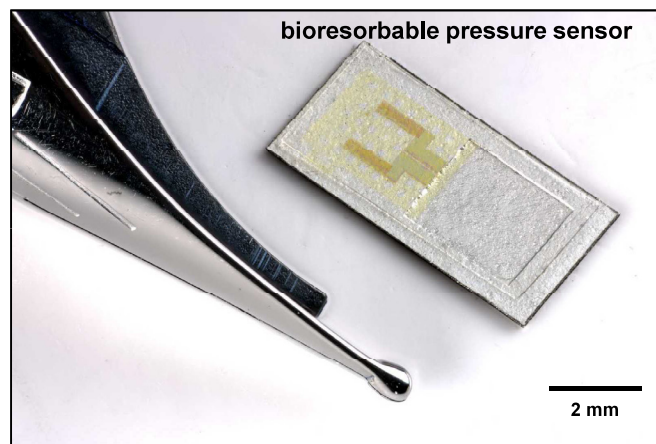
Figure S3. Biodegradable pressure sensor with Mg trench structure. Trench depth and thickness of Mg foil are ~ 40 μm and ~ 80 μm, respectively.
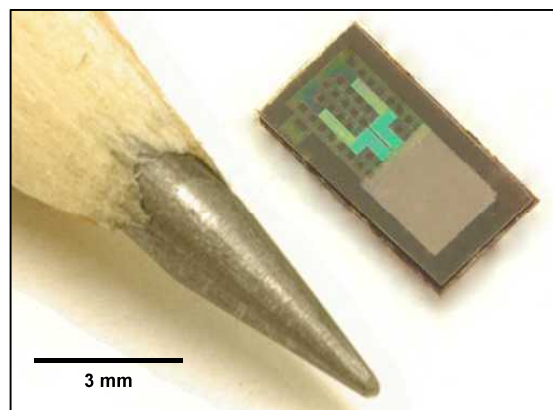
Figure S4. Image of a bioresorbable pressure sensor, with a thickness of ~110 μm, a weight of ~1 mg and overall lateral dimensions of 3 mm × 6 mm and trench dimensions of 2 mm × 2.4 mm × 40 μm.

$\varepsilon_a = 3.0 \times 10^{-3}$

$\varepsilon_a = 3.0 \times 10^{-4}$

$\varepsilon_a = 2.75 \times 10^{-3}$

$\varepsilon_a = 1.62 \times 10^{-4}$

	3.00×10^{-3}
	2.25×10^{-3}
	1.50×10^{-3}
	0.75×10^{-3}
	0.00×10^{-3}
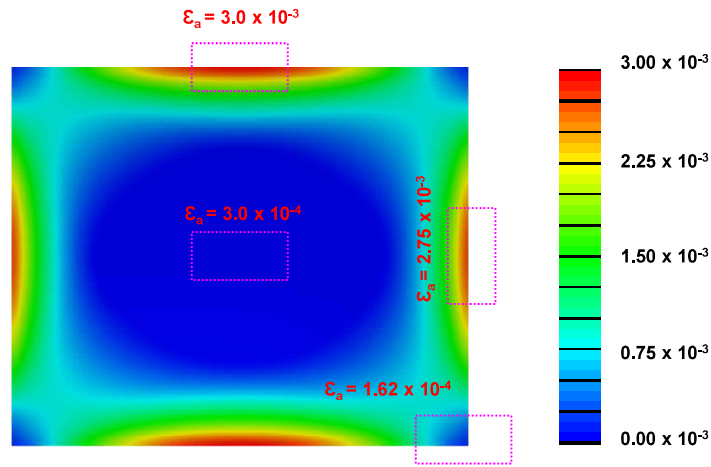
max principal strain on top surface at 70 mmHg

Figure S5. Optimization of the location of the piezoresistive serpentine sensors.

a

part of resistor coils for piezo-response

distribution of tensile strain

b 1.2 mm x 4 mm, $\varepsilon_a = 1.32 \times 10^{-3}$ 1.6 mm x 3 mm, $\varepsilon_a = 2.56 \times 10^{-3}$

%
1.78
1
0.75
0.50
0.25
0

2 mm x 2.4 mm, $\varepsilon_a = 4.84 \times 10^{-3}$ 2.2 mm x 2.2 mm, $\varepsilon_a = 3.76 \times 10^{-3}$ 4 mm x 1.2 mm, $\varepsilon_a = 0.64 \times 10^{-3}$
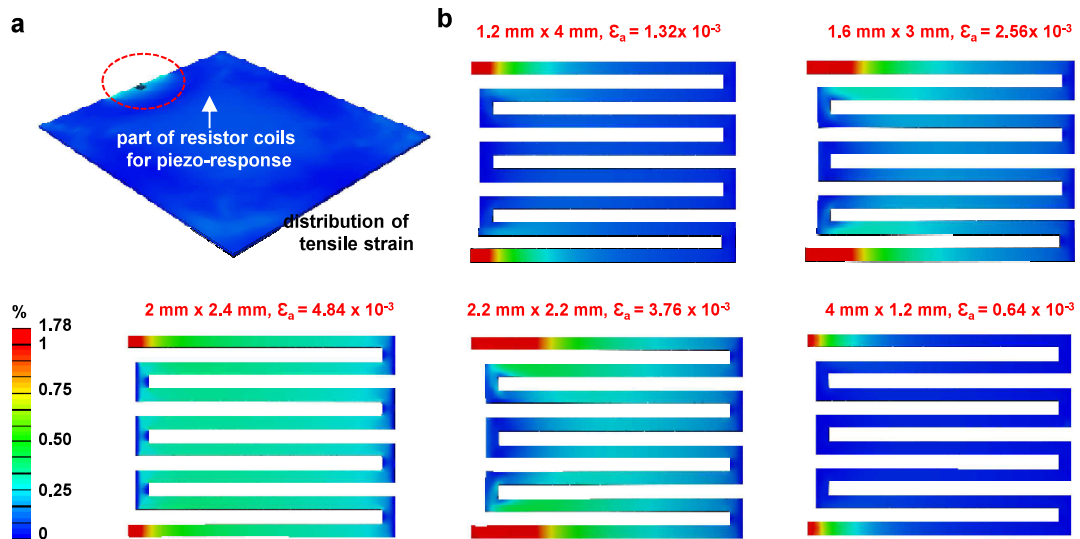
Figure S6. Optimization of trench geometry through stress-strain analysis using the finite element method (FEM). a) Full image of simulated dimension. b) Principle strain distribution around the piezoresistive serpentine sensors for various trench geometries. ε_a represents average strain on coils.
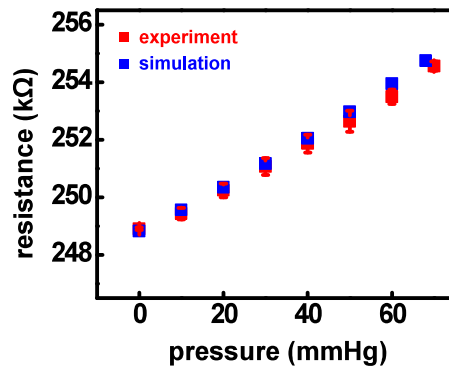
Figure S7. Piezoresistive response of the pressure sensor compared to finite element method (FEM) simulation (error bars represents standard deviations).
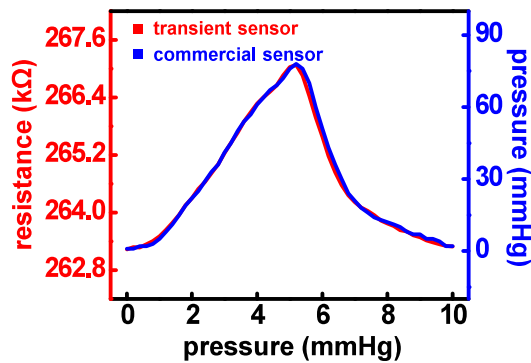
Figure S8. Calibration curve of pressure sensor with 2 mm × 2.4 mm × 40 μm dimension.
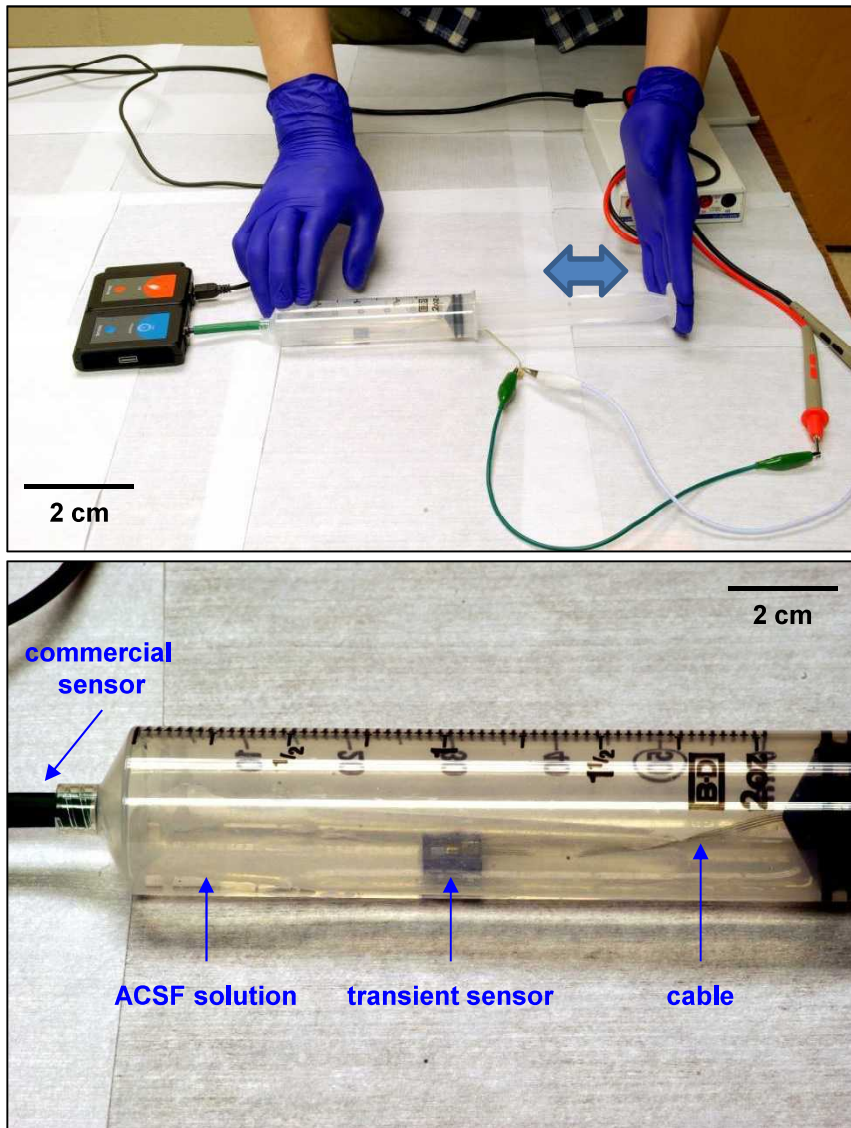
Figure S9. In vitro test of transient pressure sensor in ACSF solution.
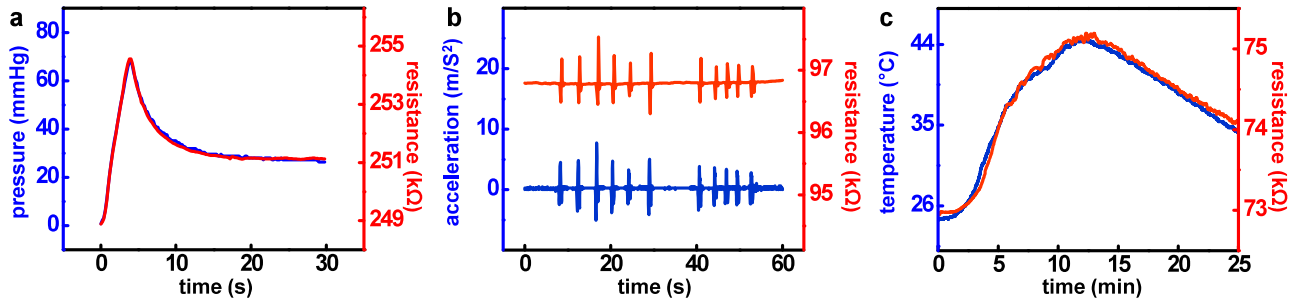
Figure S10. Calibration of resistance change to a) pressure, b) acceleration, and c) temperature.
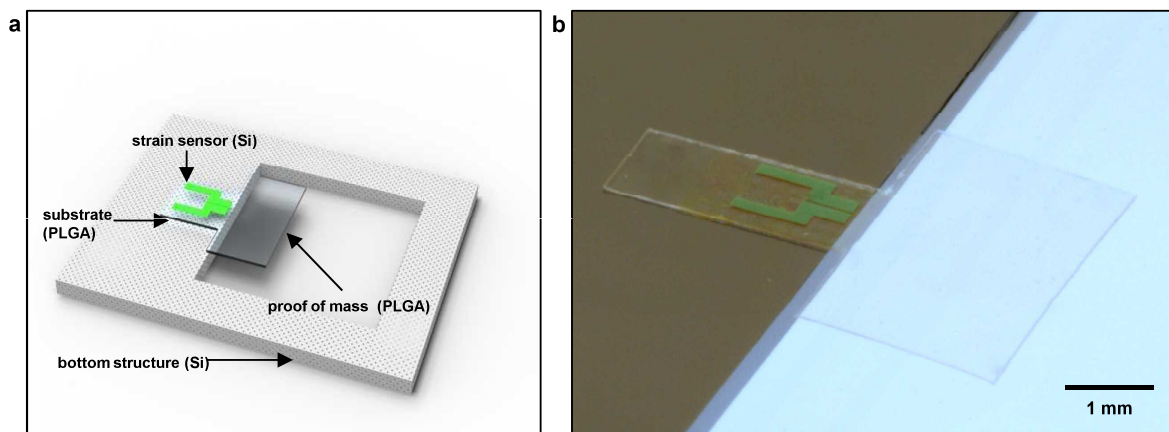
Figure S11. Transient accelerometer with Si-NM piezoresistive strain sensor. a) Materials and structure of accelerometer with PLGA proof mass. b) Image of bioresorbable accelerometer on the Si structure.
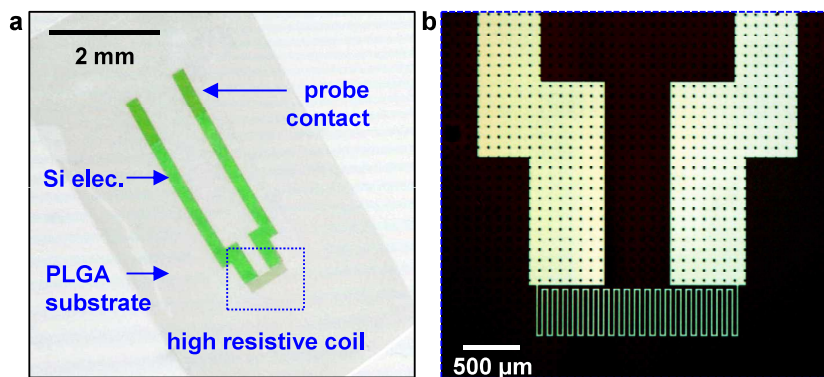
Figure S12. Bioresorbable temperature sensor on a thin PLGA film. a) Materials and structure of a thermoresistive Si temperature sensor. b) Microscope image of a dense serpentine Si-NM structure for enhanced thermoresistive response.
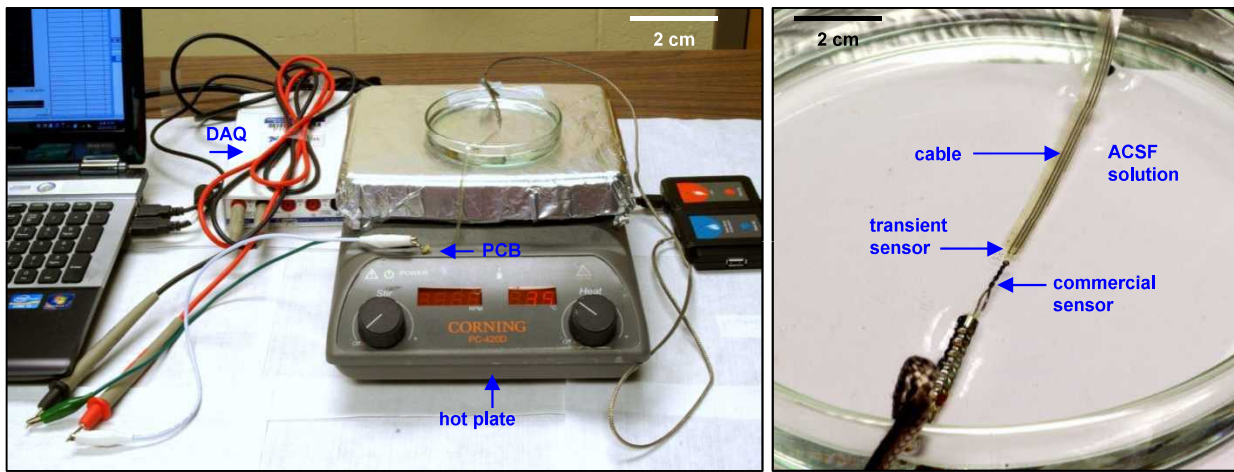
Figure S13. In vitro setup for transient temperature sensors.
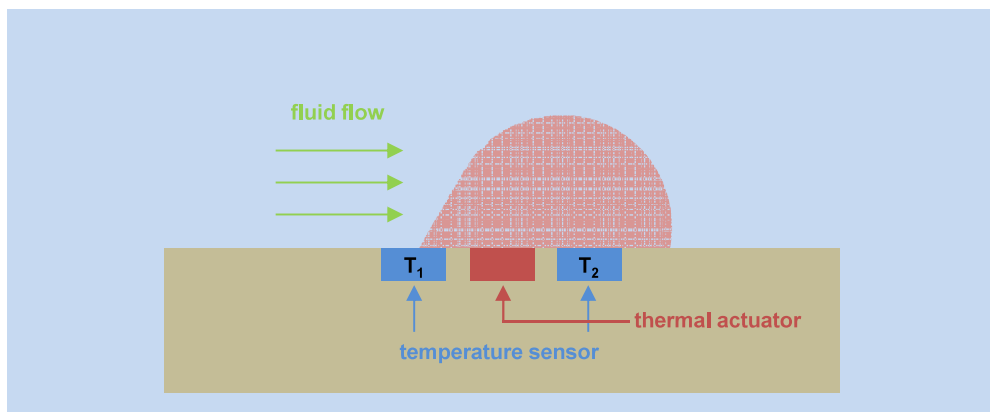
Figure S14. Principle of flow rate monitor based on a thermal actuator and a pair of temperature sensors. The difference between the temperatures recorded at the two temperature sensors (T_2-T_1) increases as the flow rate increase.
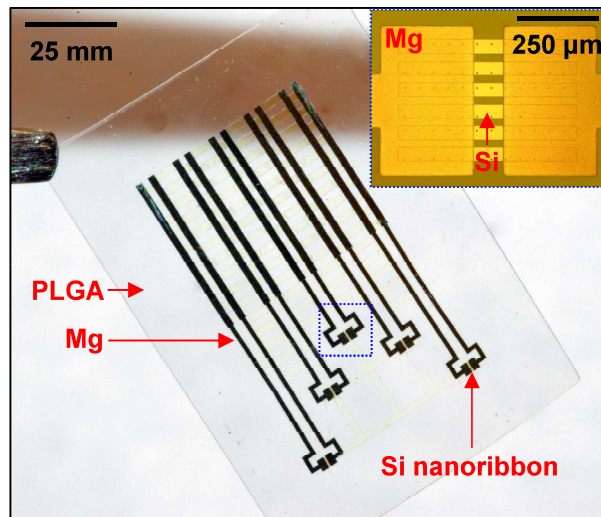
Figure S15. Bioresorbable pH sensor constructed with Si-NRs, Mg electrodes and PLGA substrates.
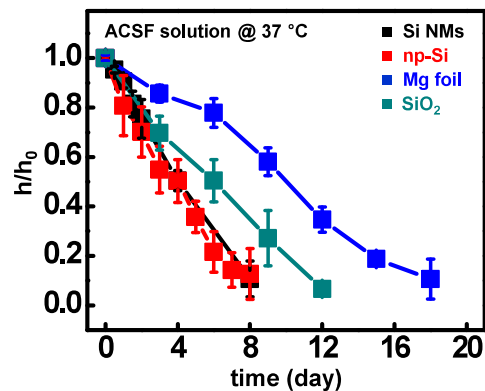
Figure S16. Hydrolysis kinetics of materials used in the bioresorbable pressure sensors. Normalized thickness (h/h_0) as a function of time during dissolution of individual materials in artificial cerebrospinal fluid (ACSF) at physiological temperature (37 °C). The initial thicknesses were 200 nm for Si nanomembranes (Si NMs), 80 μm for porous Si (p-Si), 80 μm for Mg foil, and 100 nm for SiO_2.
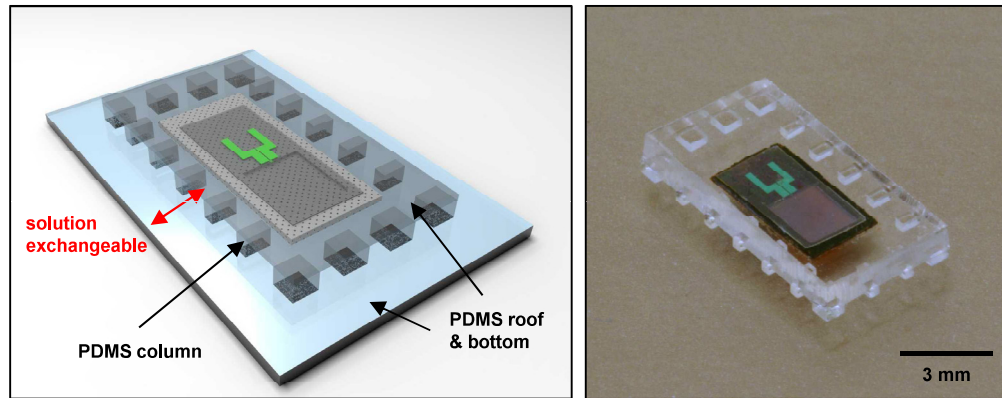
Figure S17. Schematic diagram (left) and image (right) of PDMS structure used as a simple mimic of the intracranial space.
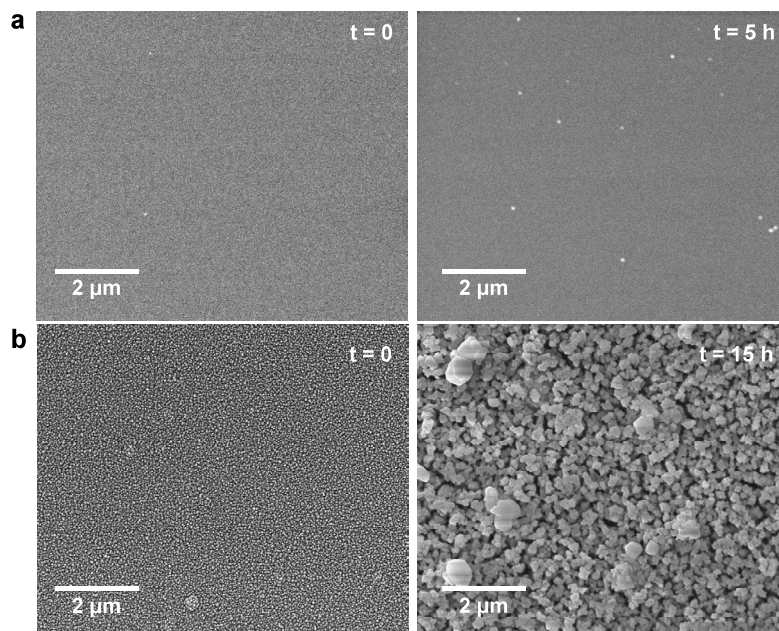
Figure S18. Scanning electron microscope (SEM) images of a) Si NMs and b) np-Si at the different stages of dissolution in buffer solution with pH 12 at 37 °C.
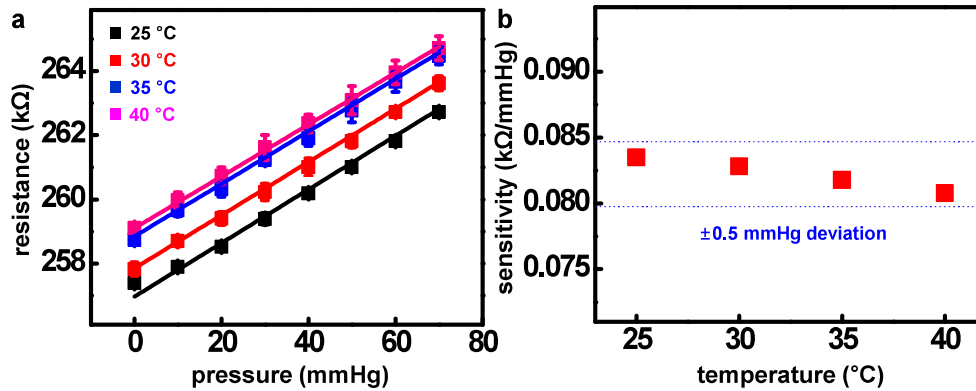
Figure S19. Calibration of the temperature dependent piezoresistivity. a) Resistivity variation to applied pressure at various temperatures (error bars represents standard deviation). b) Variation of sensitivity of resistivity to pressure associated with changes in temperatures. The change of piezoresistivity sensitivity is negligible across the expected range of brain temperatures.
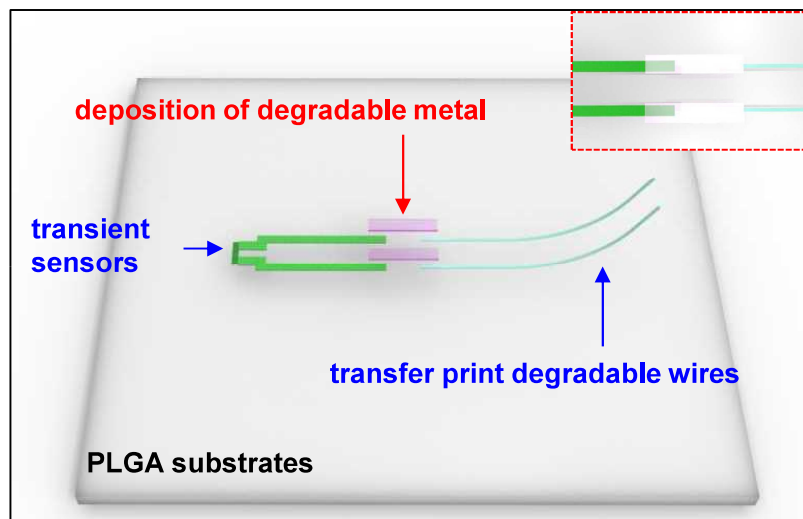
Figure S20. Strategy for interconnection between a bioresorbable device and degradable external wires on biodegradable polymer. Transfer printing the biodegradable wires (Mg or Mo) on the biodegradable polymer substrate (PLGA), and depositing dissolvable metal (Mo) between the wires and sensors yield the fully bioresorbable interface.
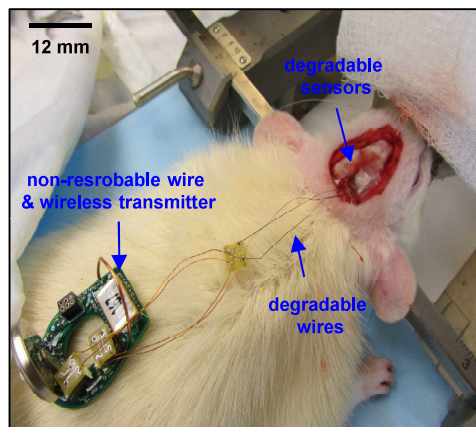
Figure S21. Image of the interface between the bioresorbable wires and the wireless transmitter.
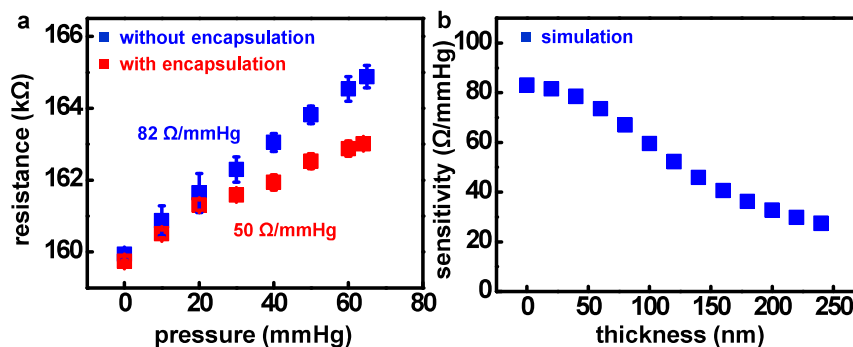
Figure S22. Effect of polyanhydride encapsulation on the response of the pressure sensor. a) Calibration curves before and after encapsulation. The calibration factor changes from 82 to 50 Ω/mmHg with 120 μm thick encapsulation (error bars represents standard deviation).   b) The thickness dependent sensitivity simulated by FEM.
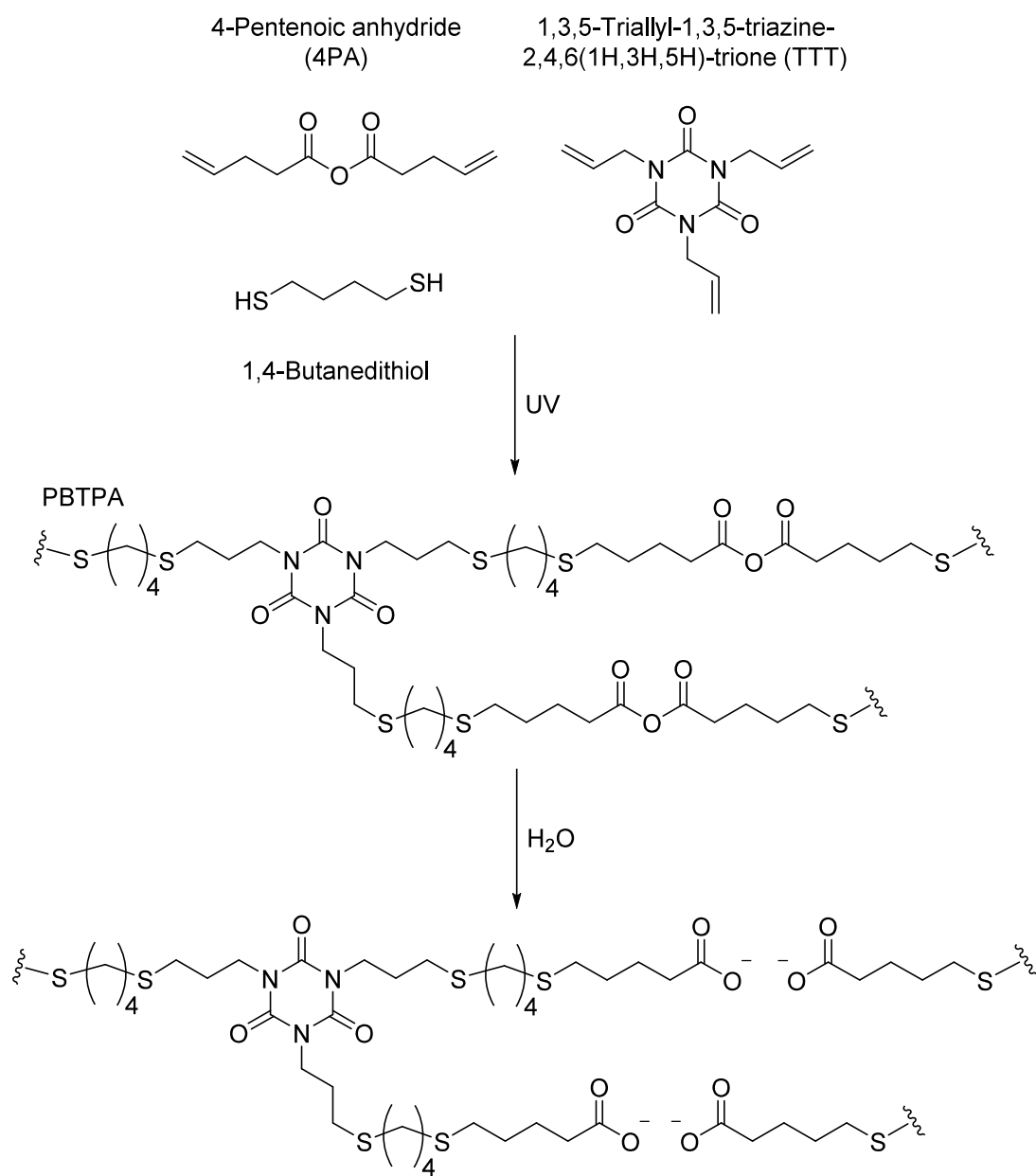
Figure S23. Chemistry of synthesis and hydrolysis of a biodegradable polymer (class of polyanhydride) for encapsulation.
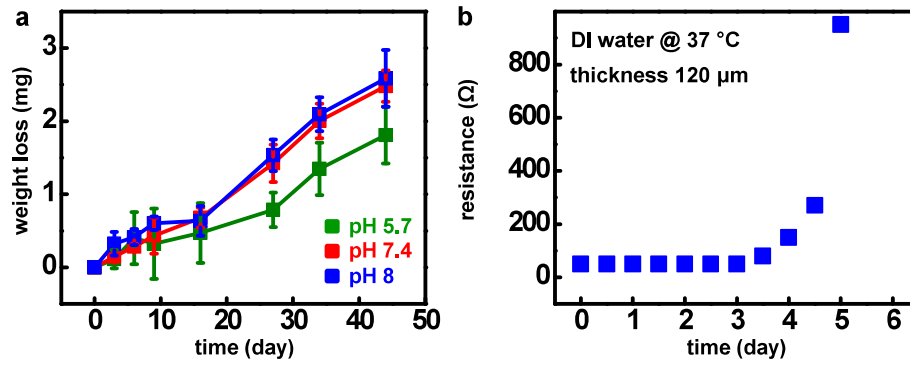
Figure S24. a) Dissolution kinetics and b) water permeability (tested by 300 nm thick Mg resistor) of polyanhydride encapsulation.
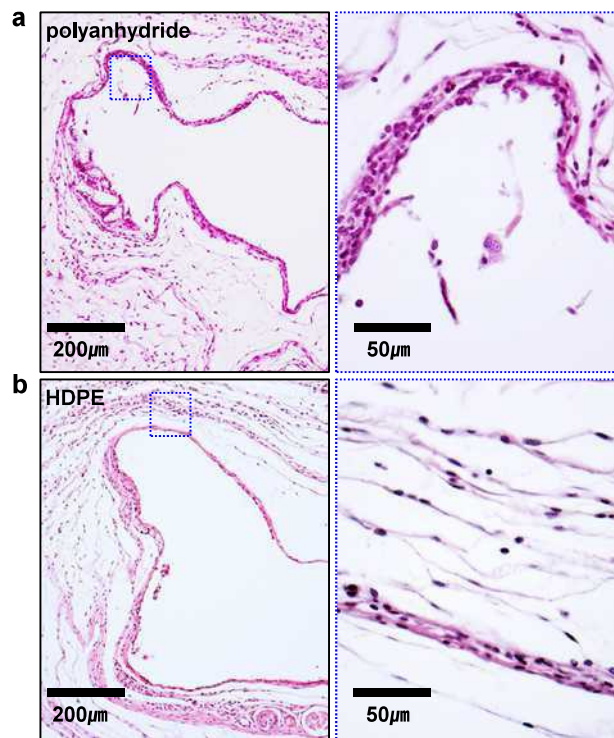
Figure S25. Hematoxylin and eosin (H&E) images of tissue around the implant site of a) polyanyhdride and b) HDPE after 14 days.
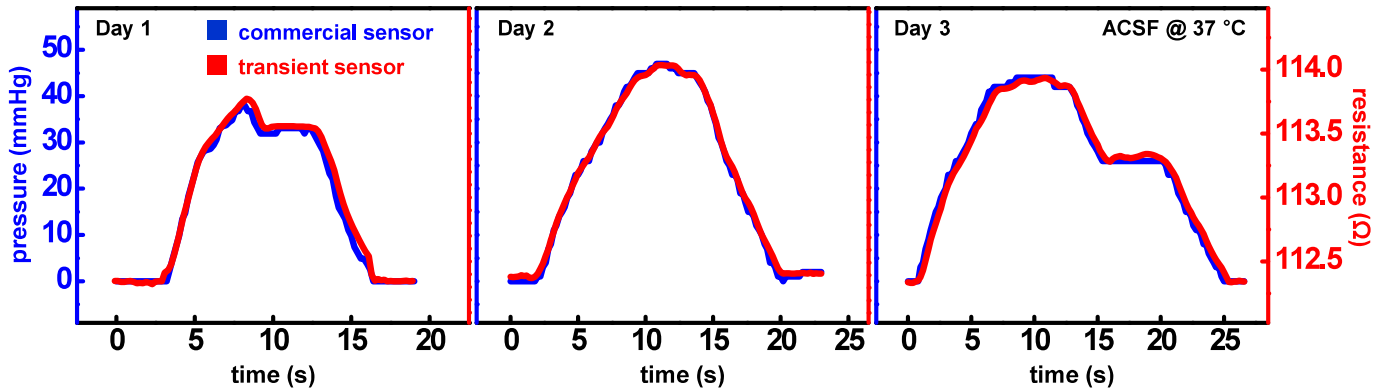
Figure S26. In vitro operation of bioresorbable pressure sensor with functional lifetime controlled with a biodegradable encapsulation layer.
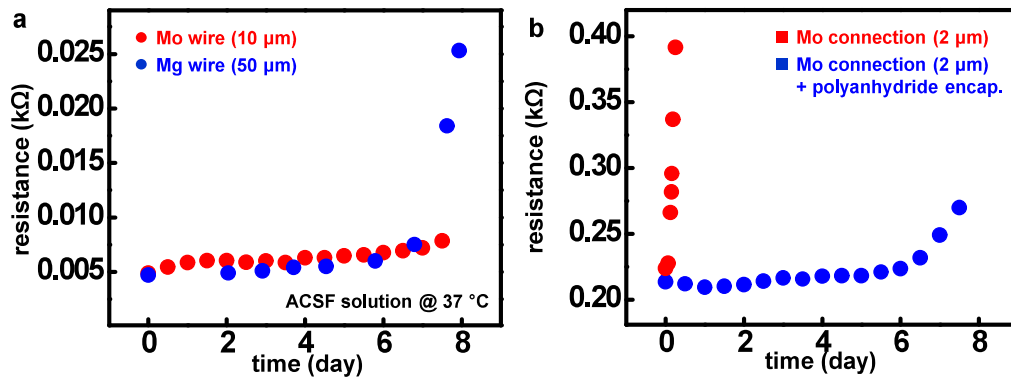
Figure S27. Effect of dissolution of metal wires and interconnects on the resistance.

a) Increases in resistance of biodegradable metal wire (Mo, 10 μm; Mg, 50 μm) in ACSF at physiological temperature for ~a week. The change in resistance is negligible (below a few ohms) for a week. The resistance of Mg wire rapidly increases after 7 days due to its higher dissolution rate compared to Mo. b) Changes in resistance of Mo interconnections (~ 2 μm) during hydrolysis in ACSF at body temperature.
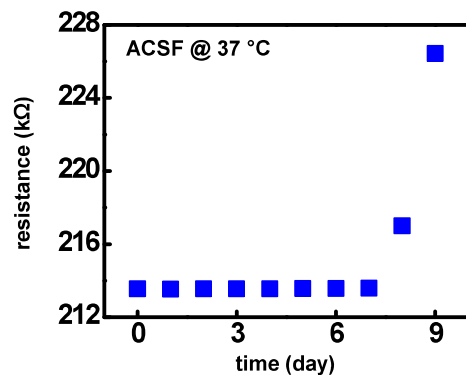
Figure S28. Resistance measurement of a pressure sensor with polyanhydride encapsulation with constant external pressure.
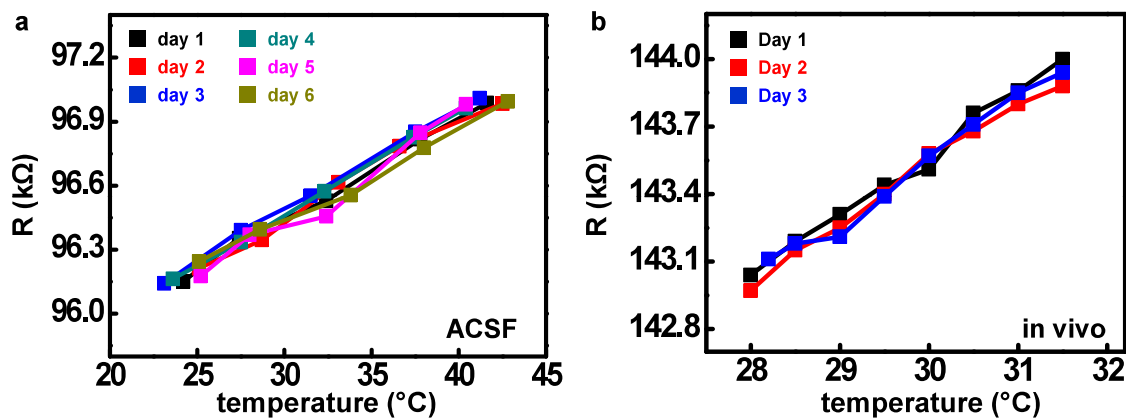

Figure S29. In vitro and in vivo demonstrations of biodegradable temperature sensors. a) Calibration curves for resistance to temperature indicate stable operation over 6 days in ACSF. b) Stable in vivo operation was demonstrated for three days. Sensors were encapsulated with a 120 μm thick layer of polyanhydride.
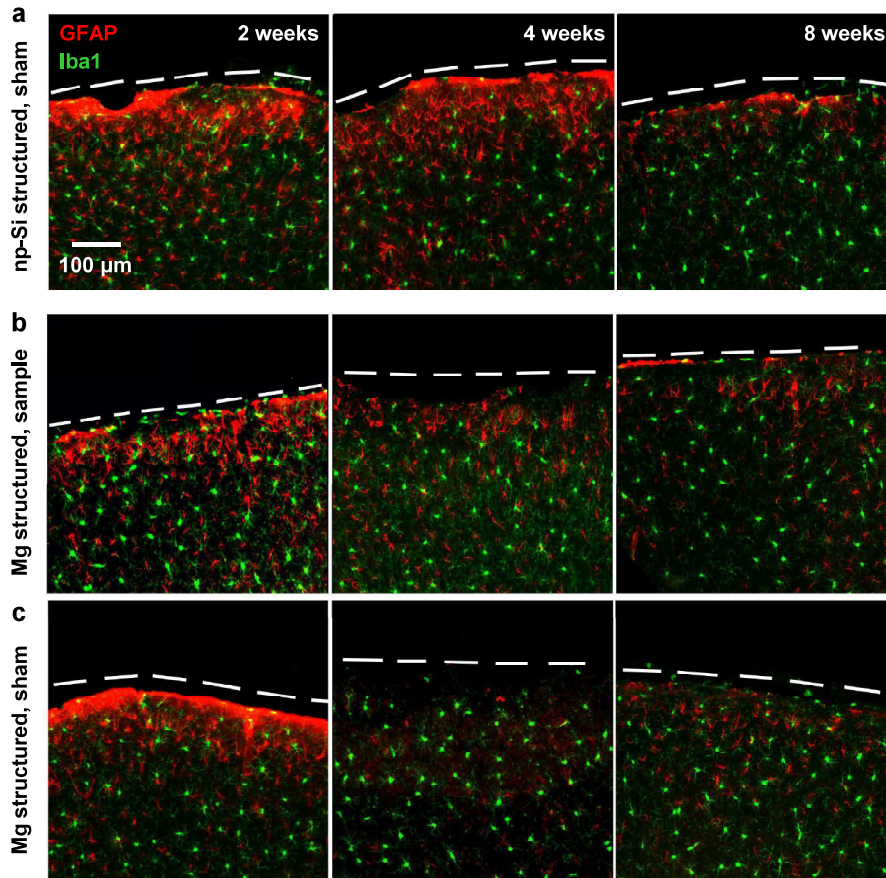
Figure S30. Confocal fluorescence images of the cortical surface. a) Series of images of the sham area (left side of brain) and the area underneath the np-Si pressure sensor (right side of brain). b) Image of the cortical surface at the site implanted with a Mg supported device and c) at the sham site.
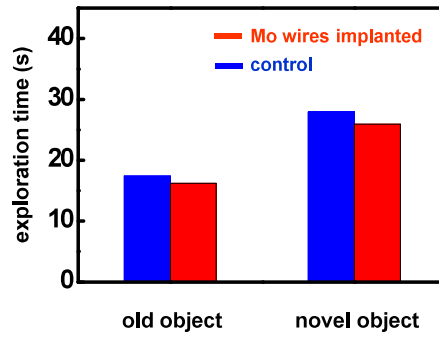
Figure S31. Animal behavior evaluation with transcutaneous wire implantation using novel object recognition test.
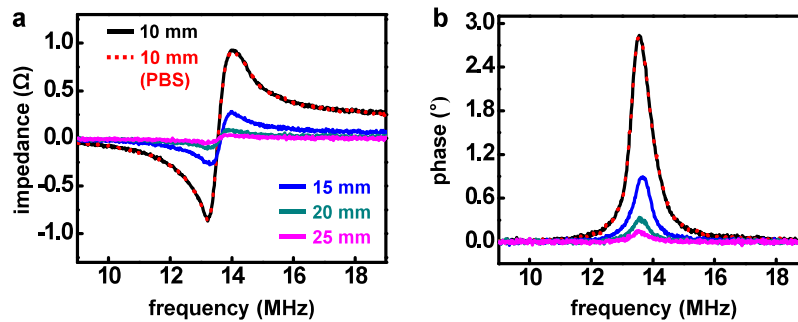

Figure S32. Frequency dependent a) impedance and b) phase of the NFC system at the different distance (black line; 10 mm, red dot; 10 mm with 2 mm barrier of phosphate buffer solution (PBS), blue line; 15 mm, cyan line; 20 mm, magenta line; 25 mm).
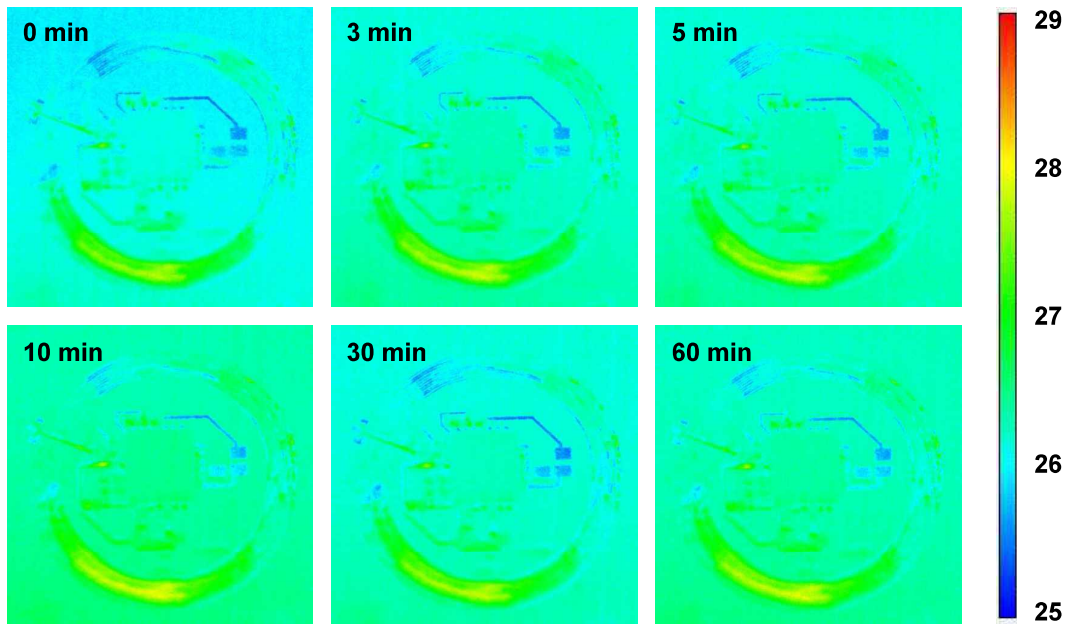
**Figure S33.** IR thermography of an NFC system during wireless operation in air.
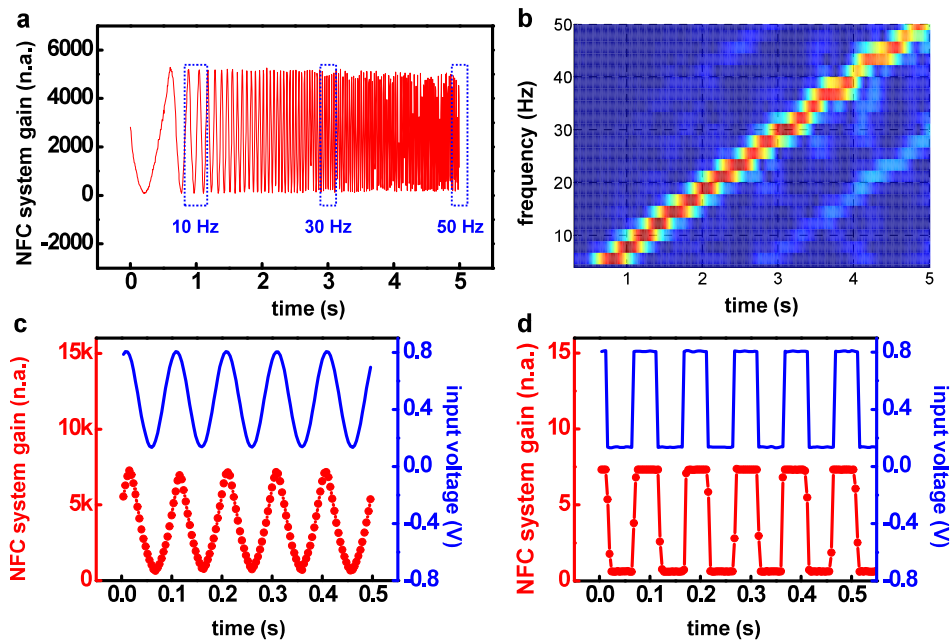
Figure S34. High sampling rate of NFC system. a) Wirelessly transmitted voltage sine waves with frequencies between 1 to 50 Hz.   Maximum sampling rate of this system is 250 Hz.   b) Spectrogram of swept sine wave in Figure 2f.   High speed data acquisition of NFC system demonstrated with c) sine and d) square wave of 10 Hz frequency. (Red dot line is the data point measured by NFC system and blue line is input signal from signal generator.)
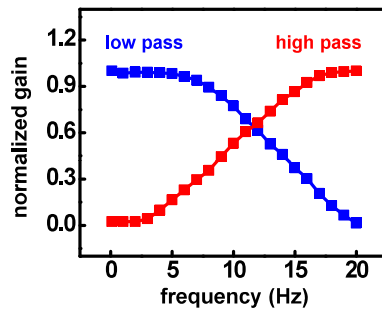
Figure S35. Gain response of programmed real-time high (red) and low (blue) pass filtering, performed by the NFC chip, as a function of frequency.
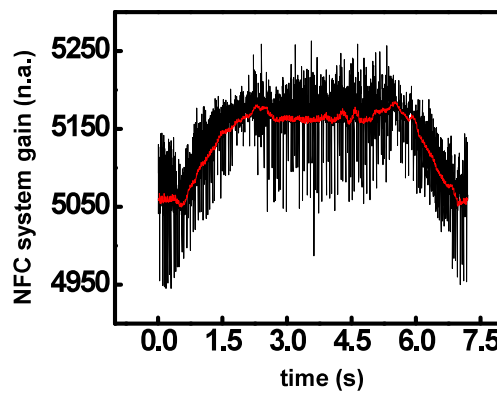

Figure S36. Comparison of filtered (red) and unfiltered (black) gain during pressure measurement. Two channels were measurement through NFC system at the same time. The filter function was loaded and performed in the chip.
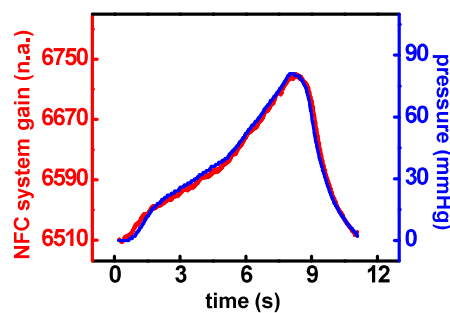
Figure S37. Response of a commercial pressure sensor (blue) and a wireless, biodegradable system (red) to time-varying pressure over a range relevant to intracranial monitoring.
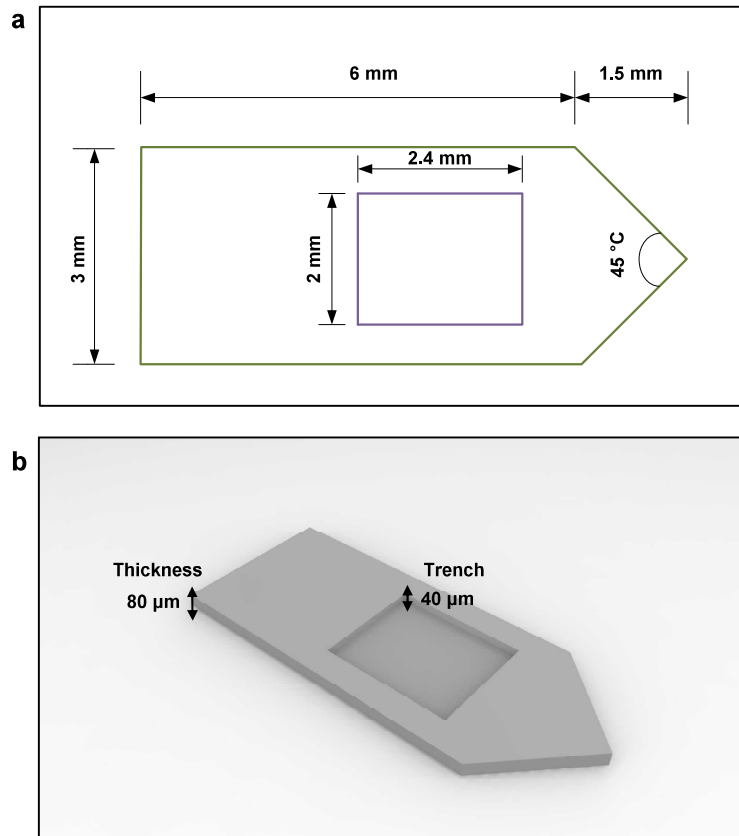
Figure S38. Geometry of needle substrates of pressure sensor. a) Lateral geometry and b) three dimensional geometry of Mg needle substrates.
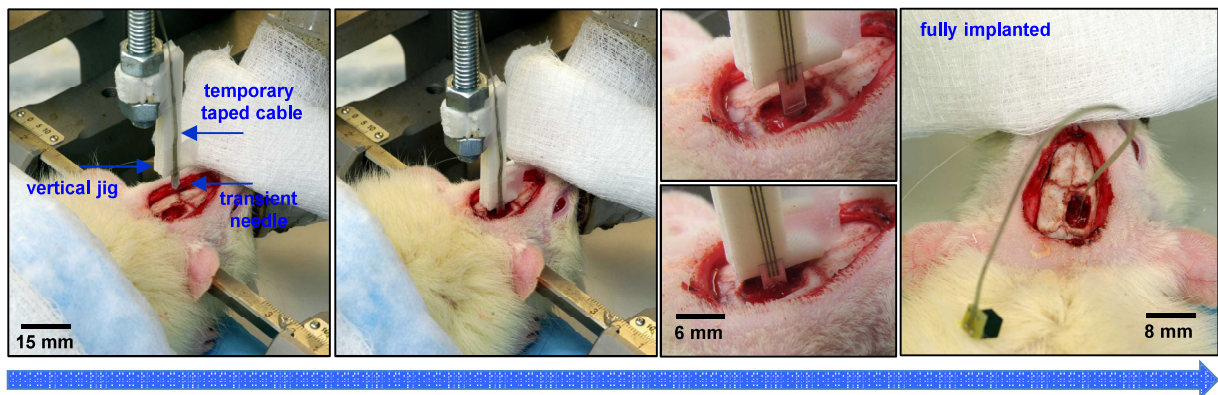
Figure S39. Surgical process for injectable form of biodegradable sensors. A needle shaped sensor was positioned with a jig. Lowering the jig causes the sharp edge of the device to penetrate into the deep brain.